




# Scanning darkfield high-resolution microendoscope for label-free microvascular imaging

HUAYU HOU,<sup>1</sup>  YUBO TANG,<sup>1</sup>  JACKSON B. COOLE,<sup>1</sup>  ALEX KORTUM,<sup>1</sup> RICHARD A. SCHWARZ,<sup>1</sup> JENNIFER CARNS,<sup>1</sup> ANN M. GILLENWATER,<sup>2</sup> PREETHA RAMALINGAM,<sup>3</sup> ANDREA MILBOURNE,<sup>4</sup> MILA P. SALCEDO,<sup>4,5</sup> KATHLEEN M. SCHMELER,<sup>4</sup> AND REBECCA R. RICHARDS-KORTUM<sup>1,\*</sup>

<sup>1</sup>Department of Bioengineering, Rice University, Houston, TX 77005, USA

<sup>2</sup>Department of Head and Neck Surgery, The University of Texas MD Anderson Cancer Center, Houston, TX 77030, USA

<sup>3</sup>Department of Pathology, The University of Texas MD Anderson Cancer Center, Houston, TX 77030, USA

<sup>4</sup>Department of Gynecologic Oncology and Reproductive Medicine, The University of Texas MD Anderson Cancer Center, Houston, TX 77030, USA

<sup>5</sup>Department of Obstetrics and Gynecology, Federal University of Health Sciences of Porto Alegre (UFCSA)/Santa Casa Hospital of Porto Alegre, Porto Alegre, Brazil

\*[rkortum@rice.edu](mailto:rkortum@rice.edu)

**Abstract:** Characterization of microvascular changes during neoplastic progression has the potential to assist in discriminating precancer and early cancer from benign lesions. Here, we introduce a novel high-resolution microendoscope that leverages scanning darkfield reflectance imaging to characterize angiogenesis without exogenous contrast agents. Scanning darkfield imaging is achieved by coupling programmable illumination with a complementary metal-oxide semiconductor (CMOS) camera rolling shutter, eliminating the need for complex optomechanical components and making the system portable, low-cost (<\$5,500) and simple to use. Imaging depth is extended by placing a gradient-index (GRIN) lens at the distal end of the imaging fiber to resolve subepithelial microvasculature. We validated the capability of the scanning darkfield microendoscope to visualize microvasculature at different anatomic sites *in vivo* by imaging the oral cavity of healthy volunteers. Images of cervical specimens resected for suspected neoplasia reveal distinct microvascular patterns in columnar and squamous epithelium with different grades of precancer, indicating the potential of scanning darkfield microendoscopy to aid in efforts to prevent cervical cancer through early diagnosis.

© 2023 Optica Publishing Group under the terms of the [Optica Open Access Publishing Agreement](#)

## 1. Introduction

Dysregulated angiogenesis provides a highly predictive biomarker for early detection of malignant progression. Many clinical studies have shown significantly increased microvessel density during the transformation of normal mucosa to invasive carcinoma in the oral cavity [1–4], cervix [5,6], Barrett’s esophagus [7] and lung [8]. In addition, morphological alterations of surface microvessels are observed during cancer progression. Several studies report altered microvessel diameter in cancerous lesions compared to normal tissue [4,8,9]. In a study of invasive squamous cell carcinoma of the lung, for example, Shibuya et al. demonstrated that the structure of microvasculature is altered from regular shapes of loops and networks to irregular dotted and spiral morphologies [8]. Increased irregularity and complexity of microvascular morphology were also observed in malignant lesions in the oral cavity [10,11], larynx [12], cervix [13] and

Barrett's esophagus [7,9,14], indicating that microvascular morphology can be an important predictive factor for early cancer detection.

A range of optical techniques have been used for *in vivo* microvascular imaging at both microscopic and macroscopic scales, and various contrast mechanisms have been studied. In fluorescence microscopy [15–21], exogenous contrast agents, such as fluorescein, are used to image blood vessels. Alternatively, label-free approaches have been developed to visualize vasculature by leveraging endogenous contrast via tissue scattering and hemoglobin absorbance, and vasculature has been visualized using laser speckle contrast imaging [22–25], optical coherence tomography (OCT) [26–33], photoacoustic imaging [34–37], narrowband imaging (NBI) [38–40], and darkfield imaging [41–44]. Nonetheless, the clinical use of these label-free modalities is usually hindered by their high cost, limited resolution, and large form factor. For example, commercially available NBI endoscopes are usually expensive and provide macroscopic imaging of the vascular network at a low resolution. OCT angiography [32,33] provides 3D microscopic images of microvessels, but image quality can suffer from motion artifacts due to low frame rates.

To extend clinical applicability to different anatomic sites, vascular imaging can be performed via thin and flexible fiber optic bundles. Confocal laser endomicroscopy is a commercially available platform obtaining high-resolution images through a coherent fiber bundle with fluorescein as a contrast agent [20,21]. The fiber bundle is placed in direct contact with the tissue epithelium and relays an optical image to the proximal end, which is imaged by an external confocal microscope. Images are displayed to clinicians on a monitor at video frame rate in real time. However, in order to highlight the vascular network, fluorescein is intravenously administered prior to imaging. Alternatively, high hemoglobin absorption in the visible spectrum can provide endogenous contrast for label-free vascular imaging in reflectance mode. However, the implementation of reflectance imaging with a fiber-optic imaging system is hindered by strong internal reflection generated at the surfaces of the fiber bundle.

In this work, we present the first demonstration of a high-resolution microendoscope integrated with scanning darkfield imaging (DF-HRME) for *in vivo* and label-free microvascular imaging. The DF-HRME images reflected light at 525 nm illumination; endogenous absorption of hemoglobin provides microvessel contrast. To reject strong internal reflection in the fiber-optic system, we implemented scanning darkfield imaging using a digital light projector (DLP) as the illumination source and a complementary metal-oxide semiconductor (CMOS) camera with a rolling shutter as the imaging sensor. The system is portable, low-cost (<\$5,500) and simple to calibrate. In addition, we designed a fiber-based imaging probe with an extended focusing depth to image subsurface microvessels. We first compare the performance of scanning darkfield imaging to non-scanning widefield imaging. We then validate the capability of DF-HRME to image microvessels in the oral cavity of healthy volunteers *in vivo*. Finally, we demonstrate the ability of DF-HRME to resolve distinct microvascular features when imaging freshly resected cervical samples with precancerous lesions. Our results suggest that microvascular imaging with DF-HRME is a promising approach to image vascular changes that accompany development of precancer and early cancer.

## 2. Methods

### 2.1. DF-HRME system design

As shown in Fig. 1(A), the DF-HRME system consists of a portable scanning darkfield microscope, a handheld imaging probe and a laptop. When imaging with the DF-HRME, a thin and flexible imaging bundle is placed directly onto the tissue epithelium. The bundle relays an optical image to the back-end optical system. High-resolution images of microvasculature are displayed to clinicians in real-time. Images of microvasculature can be shown in high contrast without the need for an exogenous contrast agent. A photo of the DF-HRME imaging setup is shown in

Fig. 1(B), with the DF-HRME in a portable case (22.9 cm × 38.1 cm × 7.62 cm). A graphical user interface (GUI) programmed in MATLAB (The MathWorks, Natick, Massachusetts) is implemented on a laptop to control the DF-HRME and display images in real-time.

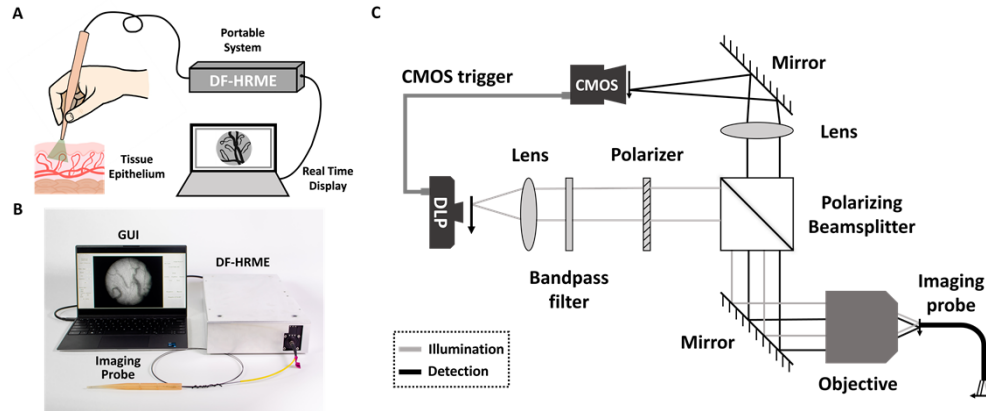


**Fig. 1.** (A) Block diagram and (B) photograph of the portable DF-HRME imaging system. The distal tip of a thin, flexible fiber optic bundle is enclosed in a 3D-printed probe holder and placed in contact with the tissue epithelium. The probe relays the image to the portable optical system at the proximal end of the bundle. The system is controlled via a GUI on a laptop; high resolution video of microvasculature is displayed in real time without the need for an exogenous contrast agent. (C) Optical diagram of the DF-HRME. Scanning darkfield illumination is used to enable reflectance imaging of microvasculature through the fiber bundle. A DLP is used to project a scanning structured illumination pattern at the proximal face of the fiber bundle; synchronized detection is performed using a CMOS camera. An offset is introduced between the illumination and detection apertures to reduce internal reflection. Arrows indicate the directions of scanning at the probe surfaces, DLP and CMOS camera. DF-HRME: scanning darkfield high-resolution microendoscope; DLP: digital light projector; CMOS: complementary metal-oxide semiconductor camera; GUI: graphical user interface.

The optical schematic of the DF-HRME is shown in Fig. 1(C). Illumination is provided using a DLP (LightCrafter 4500, Texas Instruments, Dallas, Texas). To provide contrast for imaging microvasculature, the green LED on the DLP is used with a bandpass filter (525/45 nm, FF01-525/45-25, AVR Optics, Fairport, New Jersey) to take advantage of high hemoglobin absorption. Reflected light is captured using a CMOS camera (FL3-U3-120S3C-C, Teledyne FLIR, Wilsonville, Oregon) with a rolling shutter. A sequence of illumination patterns that are complementary to detection apertures are projected; an offset between the illumination and detection apertures is programmed to reject direct internal reflection from fiber surfaces. To synchronize the two aperture sequences, a triggering signal is sent from the DLP to the camera. The projected patterns are collimated by a lens ( $f = 100$  mm, AC254-100-A, Thorlabs, Newton, New Jersey) and focused through a 10× objective (#86-818, Edmund Optics, Barrington, New Jersey) onto the proximal end of an imaging probe. The imaging probe, consisting of a coherent fiber bundle and a gradient-index (GRIN) lens attachment (described in Section 2.3 in detail), further relays the focused illumination patterns to the tissue. Darkfield signal collected by the imaging probe is collimated and focused onto the CMOS camera by a tube lens ( $f = 100$  mm, AC254-100-A, Thorlabs, Newton, New Jersey). Two mirrors (PF10-03-G01, Thorlabs, Newton, New Jersey) are mounted onto two right-angle mirror mounts (KCB1, Thorlabs, Newton, New Jersey) for precise scanning darkfield alignment. In addition to darkfield imaging, we also used a linear polarizer (LPVISE100-A, Thorlabs, Newton, New Jersey) and a polarizing beamsplitter

cube (CCM1-PBS251, Thorlabs, Newton, New Jersey) to further suppress background signal due to internal reflection. The total cost of goods to assemble the DF-HRME was less than \$5,500.

## 2.2. Synchronization and scanning darkfield imaging

A major barrier for reflectance imaging through a fiber bundle is the presence of strong internal reflections from its surfaces. In this section, we describe the detailed design of the illumination and detection aperture sequences to enable darkfield imaging (Fig. 2(A)). In rolling shutter mode, a detection line aperture scans the entire CMOS sensor at a fixed row frequency to complete one readout, as illustrated by the blue parallelogram filled with diagonal lines in the top panels of Fig. 2(A). During widefield imaging, no illumination aperture sequence is provided and the entire field of view (FOV) is illuminated while the rolling shutter scans across the CMOS sensor (top left panel, Fig. 2(A)). The spatial-temporal overlap of illumination with the detection aperture sequence results in strong background signal due to internal reflection from the fiber bundle surfaces, significantly degrading image contrast. During darkfield imaging, DLP illumination patterns are synchronized with the rolling shutter to achieve scanning darkfield imaging (top right panel, Fig. 2(A)). The spatiotemporal coordination of illumination and detection aperture sequences for non-scanning widefield imaging and scanning darkfield imaging is also demonstrated in Visualization 1. The resulting background images (when illumination is on and no target is imaged with fiber in air) in Fig. 2(A) show that darkfield illumination significantly suppresses internal reflection. This is confirmed by Fig. 2(B), showing that the intensity of the background is reduced by 83% in darkfield imaging compared to widefield imaging.

The detailed implementation of darkfield illumination is in principle similar to our previous work on a line-scanning confocal HRME [45,46]. By adjusting the shutter time, the size of the detection aperture (or the number of rows in the CMOS sensor that are concurrently exposed) can be controlled:

$$D = T * f, \quad (1)$$

where  $D$  is the width of the detection aperture,  $T$  is the shutter time, and  $f$  is the row scanning frequency of the CMOS sensor. In our current DF-HRME setup, a line aperture width of 120 pixels is used, which corresponds to 30  $\mu\text{m}$  at the proximal end of the imaging probe. As previously discussed [45,46], it is impractical to achieve a one-to-one match between the illumination aperture and the detection aperture. The reasons are that the DLP refresh rate (1.3 kHz) is significantly lower than the scanning rate of CMOS rolling shutter (49 kHz), and the number of illumination patterns that can be stored in DLP is limited. To address the disparity of scanning in illumination and detection, each illumination pattern corresponds to a series of detection apertures when using scanning darkfield imaging (top right panel, Fig. 2(A) and Visualization 1). In DF-HRME, 24 binary patterns are preloaded in the DLP memory buffer and projected to match 3000 distinctive detection apertures (the total number of rows in the CMOS sensor) in a single frame acquisition. The size and duration of projected illumination patterns are adjusted to ensure a spatiotemporal offset between the illumination aperture sequence and detection aperture sequence, with the timespan of the entire illumination sequence matching the single-frame acquisition time. By adjusting the aperture width and the spatiotemporal offset when imaging the oral cavity of normal volunteers, we observed that the overall signal level changed, but there were no notable changes in contrast or resolution. In the current study, we empirically selected the aperture design that achieves high signal levels while ensuring that there is no overlap between illumination and detection aperture. A sequence of illumination line pairs is used in the current DF-HRME setup. The line widths are  $4D$  and their centers are separated by  $8D$  in Fig. 2(A), corresponding to 120  $\mu\text{m}$  and 240  $\mu\text{m}$  at the proximal end of the imaging probe, respectively.

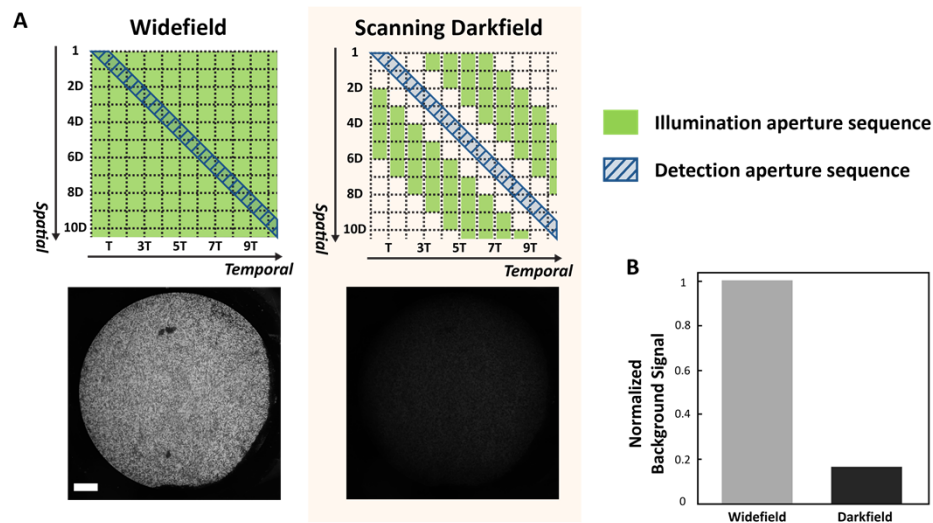


**Fig. 2.** Scanning darkfield imaging is implemented to suppress background signal due to strong internal reflection from fiber bundle surfaces. (A) Schematic of the spatiotemporal coordination of illumination and detection aperture sequences for non-scanning widefield imaging and scanning darkfield imaging. In widefield imaging, the entire field of view is illuminated by the DLP as the detection aperture (width  $D$  and shutter time  $T$ ) of the CMOS camera scans across the entire sensor to capture image information. In scanning darkfield imaging, a sequence of illumination line pairs (width  $4D$  and spaced by  $8D$  from center to center) is scanned across the field of view synchronized with but spatially offset from the detection aperture sequence. The corresponding background images captured with no sample are shown below; scanning darkfield imaging suppresses internal reflection. (B) Normalized background signal for the DF-HRME system in widefield and scanning darkfield modes. (Scale bar:  $100\ \mu\text{m}$ )

### 2.3. Design and characterization of imaging probes

To obtain in-focus images of subsurface vasculature in the oral cavity, a GRIN lens was used to extend the working distance of a bare fiber bundle. As shown in Fig. 3(A), a 1 mm diameter GRIN lens (1050-002176, Inscopix, Mountain View, California) is attached to the distal end of a coherent fiber bundle ( $790 \pm 50\ \mu\text{m}$  circular field of view, FIGH-30-850N, Fujikura, Tokyo, Japan) to relay the fiber focal plane to an imaging plane below the tissue surface. A range of probe imaging depths ( $d_2$ ) can be achieved by adjusting the working distance at the fiber side ( $d_1$ ) during fabrication. To guide the fabrication process, we measured the relationship between  $d_1$  and  $d_2$ ; results are shown in Fig. 3(B). During the experiment, optical epoxy was applied to fill the gap between the fiber bundle and the GRIN lens. Water immersion was used on the object side to simulate the imaging depth in biological tissue. Based on the calibration curve in Fig. 3(B), three imaging probes with imaging depths of  $70\ \mu\text{m}$ ,  $170\ \mu\text{m}$  and  $270\ \mu\text{m}$  were fabricated. The imaging depth of the probe approximately indicates the depth of the vessels that are in focus within the measured depth of field ( $40\ \mu\text{m}$ ) of the imaging probe. The measured FOV of these probes are  $764\ \mu\text{m}$ ,  $790\ \mu\text{m}$  and  $819\ \mu\text{m}$  diameter respectively, indicating minimal magnification changes vs. imaging depths. The resolution for all probes is  $\sim 4\ \mu\text{m}$ , which is limited by the size of fiber cores.

To fabricate a fiber probe with extended imaging depth that can be used for *in vivo* imaging, the GRIN lens is housed within hypodermic tubing that has a 12.7 mm length, 1.5 mm outside diameter and 1 mm inner diameter. Medical-grade optical epoxy (MED-301, Epoxy Technology



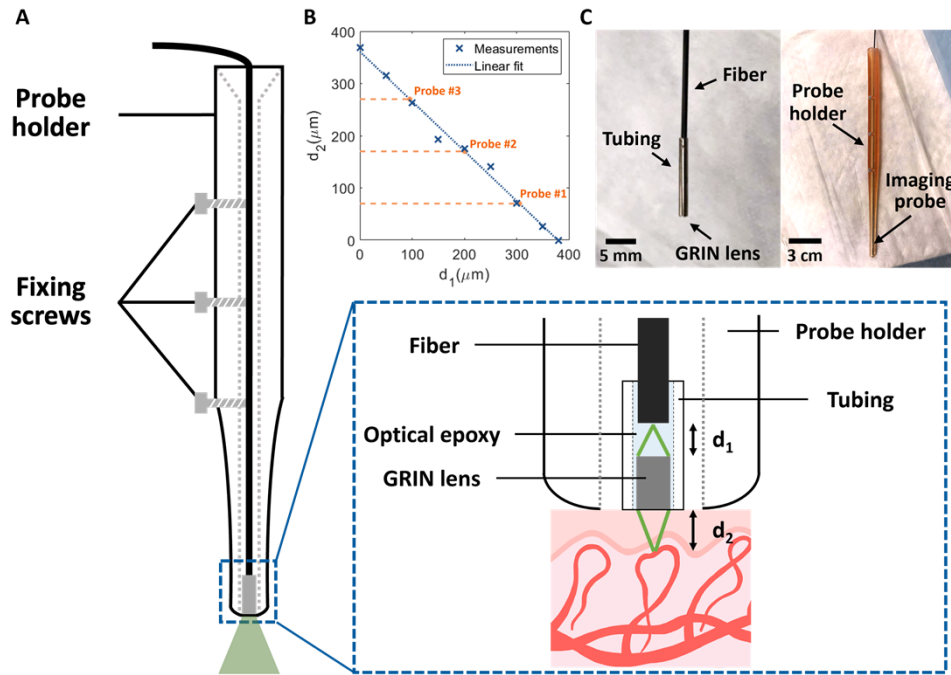


**Fig. 3.** Design and characterization of sub-surface imaging probes. (A) Schematic of the imaging probe inserted in a probe holder. Inset shows detailed design of the distal end of the imaging probe. A GRIN lens is epoxied to the distal tip of the bundle to extend the focusing depth. (B) Experimental measurements demonstrate the relationship between probe imaging depth ( $d_2$ ) and the distance between the fiber bundle and the GRIN lens ( $d_1$ ) for all imaging depths (blue dashed line), and for three imaging probes designed to image at depths of 70, 170 and 270  $\mu\text{m}$  beneath the tissue surface (orange dashed line). (C) Photograph of imaging probe before (left) and after (right) insertion into a 3D-printed probe holder to facilitate *in vivo* imaging.

Inc, Billerica, Massachusetts) is applied and cured inside the tubing to provide refractive index matching and to seal the probe. The picture of the fabricated imaging probe with affixed GRIN lens is shown in the left panel of Fig. 3(C). The imaging probe retains the flexibility and the small form factor of the tip, ensuring its applicability in different anatomic sites. When performing *in vivo* imaging, the imaging probe is inserted into a 3D-printed probe holder for steadier movement control (Fig. 3(C), right panel). The probe holder was printed using Form 3B (Formlabs, Somerville, Massachusetts) with fully biocompatible Surgical Guide Resin.

#### 2.4. *In vivo* imaging of oral cavities of healthy volunteers

*In vivo* imaging using DF-HRME was performed in the oral cavities of healthy adult volunteers at Rice University. The study was approved by the Institutional Review Board of Rice University. Written informed consent was obtained from all participants. Imaging probes underwent standard cleaning and high-level disinfection prior to each use. When performing *in vivo* imaging, the imaging probe was placed in gentle contact with the tissue at different anatomic sites within the oral cavity, including floor of mouth, lip, ventral tongue, lateral tongue, gingiva and buccal mucosa. Real-time images of microvasculature were displayed on a laptop screen using the MATLAB GUI. No contrast agent was applied during imaging. A background image was

acquired prior to imaging, and background subtraction was performed automatically during imaging to remove residual internal reflection background and further improve image contrast.

Using a probe with an imaging depth of 70  $\mu\text{m}$ , we compared darkfield and widefield images from the same anatomic regions. This was achieved by recording successive image frames from the same location with darkfield and widefield illumination patterns projected using the DLP. The imaging probe was placed approximately perpendicular to the tissue epithelial surface to ensure that the entire imaging surface was in contact with the tissue. Minimal pressure was applied to the tissue to avoid impeding blood flow in the microvasculature. A decrease in the contrast of microvasculature was observed when the pressure was significantly increased during imaging. Widefield and darkfield frames were captured sequentially within a few seconds while the imaging probe was held in position. Therefore, similar contact pressure and angle were maintained when acquiring widefield and darkfield image pairs. System parameters were adjusted to match the brightness of widefield images and corresponding darkfield images. Image pairs from different anatomic sites within the oral cavity were acquired and image quality was compared for the two modalities. To compensate for motion between successive frames during *in vivo* imaging, image registration was performed and a 400  $\mu\text{m}$  by 400  $\mu\text{m}$  region of interest (ROI) was selected for each image pair.

To facilitate evaluation of microscopic features, we first applied a Gaussian filter to the images to remove the intrinsic fiber bundle pattern. We then linearly adjusted the brightness of the images to be at the same level, and linearly enhanced the image contrast. The same image processing procedure, including background subtraction, image smoothing, brightness adjustment, and contrast enhancement, were applied to widefield and darkfield image pairs. Line profiles at the same location were plotted to compare image contrast. Vasculature contrast was calculated using the Michelson contrast formula:

$$\text{Contrast} = \frac{I_b - I_v}{I_b + I_v}, \quad (2)$$

where  $I_b$  and  $I_v$  represent the intensity of the background and vasculature, respectively.

In order to evaluate darkfield system performance at different imaging depths, additional *in vivo* imaging of oral sites in healthy volunteers was performed using the DF-HRME with a bare fiber bundle (no GRIN lens; 0  $\mu\text{m}$  imaging depth) and with imaging probes with extended imaging depths of 70  $\mu\text{m}$ , 170  $\mu\text{m}$  and 270  $\mu\text{m}$ . All images were processed using the same image processing procedure described above except the contrast enhancement process. Here we used adaptive histogram equalization instead of the linear enhancement method to improve the image contrast. To evaluate the difference in image quality at different imaging depths, line profiles were plotted across a representative vessel in each image.

## 2.5. Clinical imaging of *ex vivo* cervical specimens

To assess the potential of DF-HRME imaging to image changes in microvasculature associated with development of cervical precancer, we performed *ex vivo* imaging of freshly resected cervical specimens containing lesions suspicious for cervical precancer. The study was conducted at The University of Texas MD Anderson Cancer Center (MD Anderson). The protocol was approved by the Institutional Review Boards of MD Anderson and Rice University. Patients who were scheduled to undergo LEEP (loop electrosurgical excision procedure) for treatment of cervical dysplasia, who were 18 years of age or older, and who had a negative pregnancy test were eligible for the study. Written informed consent was obtained from all participants.

Imaging probes underwent standard cleaning and high-level disinfection prior to each use. Following the LEEP, the removed cervical specimen was immediately imaged using the DF-HRME. The tissue surface was cleaned using sterile swabs and saline to remove surface debris. DF-HRME imaging in scanning darkfield mode was then performed without any contrast agent. To evaluate image quality at different imaging depths, probes with imaging depths of 0  $\mu\text{m}$ , 70  $\mu\text{m}$ , 170  $\mu\text{m}$  and 270  $\mu\text{m}$  were used. The position of the DF-HRME probe tip was recorded

throughout the imaging procedure using a video camera. Images from DF-HRME and the video camera were saved with time stamps, which were used to correlate DF-HRME images to the corresponding locations of the imaged sites. After DF-HRME imaging, the cervical specimen was sent to the pathologist within the expected time for histopathological diagnosis per standard of care. The DF-HRME images were correlated to the standard-of-care histopathology diagnosis and corresponding histopathology images based on their spatial locations as the gold standard.

### 3. Results

#### 3.1. Widefield vs scanning darkfield imaging

Figure 4 compares widefield and darkfield images obtained at various anatomic sites within the oral cavity of a healthy volunteer. As shown in Fig. 4(A), the widefield images exhibit significantly lower contrast compared to darkfield images at all anatomic sites. Scanning darkfield imaging enabled the visualization of some microvascular features which were difficult to observe using widefield imaging (indicated by red arrows). Intensity profiles were plotted along the line scans (red dotted lines) at the same locations in widefield and darkfield images. As shown in the intensity profiles, vessels are clearly resolved in darkfield images. In comparison, vascular contrast was considerably lower in widefield images, and some microvessels cannot be distinguished from the background. Contrast improvement was consistent across different anatomic sites within the oral cavity. Figure 4(B) shows a quantitative comparison of contrast for an additional 25 representative microvessels. The results demonstrate that scanning darkfield imaging consistently provides enhanced contrast for all microvessels, with an average 3-fold improvement in contrast compared to widefield imaging.

#### 3.2. In vivo oral imaging with multiple imaging depths

To assess the capability of the DF-HRME to resolve vasculature beneath the tissue surface, we performed DF-HRME imaging using probes with different imaging depths. Four imaging probes were utilized to image different anatomic sites within the oral cavities of healthy volunteers. A total of 20 healthy volunteers were enrolled in this study. Representative DF-HRME images with intensity line profiles of selected microvessels (red arrows) are shown in Fig. 5. When using a bare fiber bundle (0  $\mu\text{m}$  imaging depth), oral vasculature was observed but was out of focus at all anatomic sites. The microvessels appeared as dark shadows with diffuse borders. At an imaging depth of 70  $\mu\text{m}$ , the morphology of microvessels was clearly resolved with improved resolution. At this depth, hairpin-like capillaries were observed in images from all anatomic sites, and the loop shapes, which were not distinguishable when using 0  $\mu\text{m}$  imaging depth, were well discerned. At 70  $\mu\text{m}$  imaging depth, the branching vessels observed in the floor of mouth were also better defined with sharper edges. The improvement in image quality was further confirmed by intensity line profiles through representative vessels. When using the imaging probe with a 170  $\mu\text{m}$  imaging depth, vascular morphology was resolved with good focus. However, when imaging depth was extended to 270  $\mu\text{m}$ , only out-of-focus vessels were observed in images from all oral anatomic sites; this is confirmed by the corresponding line profiles. Overall, these results demonstrate that microvasculature images of high quality are obtained from the oral cavity with DF-HRME imaging depths of 70  $\mu\text{m}$  and 170  $\mu\text{m}$ .

As shown in Fig. 5, a variety of vascular features were observed across different oral anatomic sites. When using the imaging probe with a 70  $\mu\text{m}$  imaging depth, large branching and elongated vessels (indicated by blue arrows) were observed in images from the floor of mouth, as shown in Fig. 5(G). At this depth, fine hairpin capillaries (indicated by green arrows) were observed at other oral anatomic sites, which are characterized by one ascending and one descending branch forming a small loop (Figs. 5(H)–5(L)). Hairpin capillary loops observed in images from the gingiva reveal shorter tails (Fig. 5(K)) compared to other anatomic sites. Different microvascular



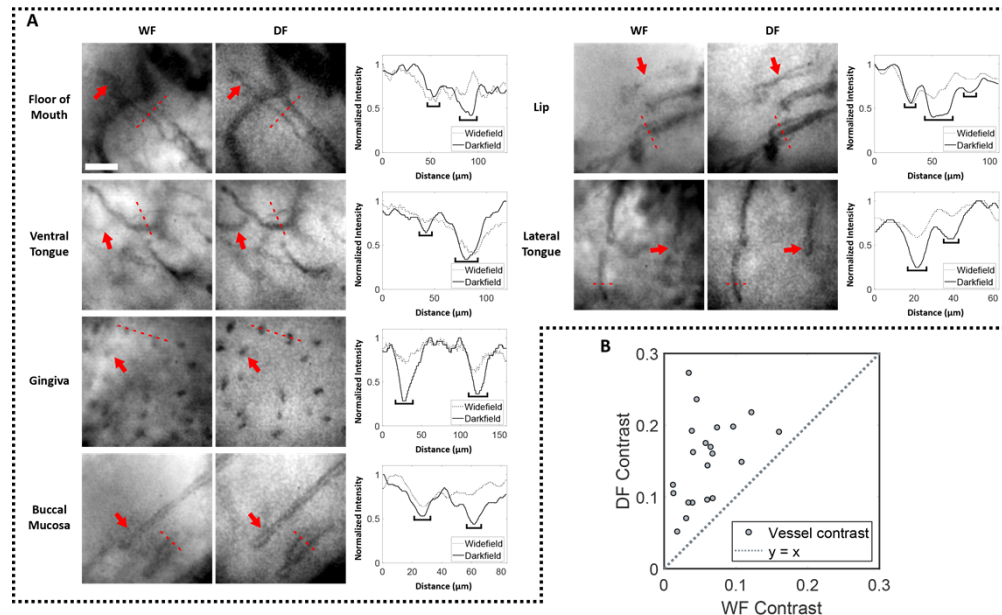


**Fig. 4.** Scanning darkfield images consistently shows improved image contrast compared to widefield images. (A) Comparison of representative images acquired using widefield imaging and scanning darkfield imaging at different anatomic sites in the oral cavity of a healthy volunteer. Images were acquired using a probe with a 70  $\mu\text{m}$  imaging depth. Corresponding intensity profiles along the red dashed lines are plotted for each image pair. Red arrows indicate the microvascular features that are clearly resolved in darkfield images but not distinguishable in widefield images. Black brackets denote vessels resolved in darkfield images. (B) Relationship between widefield and darkfield image contrast from 25 randomly selected microvessels. Each point indicates the contrast of one microvessel. WF: widefield imaging; DF: scanning darkfield imaging. (Scale bar: 100  $\mu\text{m}$ )

features can also be observed at the same anatomic site when imaging at different depths. In images of the lip, ventral tongue and lateral tongue, hairpin capillary loops were visualized at an imaging depth of 70  $\mu\text{m}$  (Figs. 5(H)–5(J)), and branching vessels were observed at these anatomic sites at an imaging depth of 170  $\mu\text{m}$  (Figs. 5(N)–5(P)). These results show that at various oral anatomic sites within the oral cavity, DF-HRME reveals different subepithelial microvascular features with high spatial resolution.

### 3.3. *Ex vivo* imaging of cervical specimens

To evaluate the capability of DF-HRME to visualize microvascular structures at varied depths in neoplastic and non-neoplastic cervical lesions, we performed DF-HRME imaging of *ex vivo* cervical specimens excised during LEEP. A total of ten patients were enrolled in this study. Figure 6 shows representative DF-HRME images from ten cervical LEEP specimens when imaging at four depths. For cervical tissue, microvascular patterns were in better focus at all anatomic sites using probes that focus at depths of 0 and 70  $\mu\text{m}$ , compared to depths of 170 and 270  $\mu\text{m}$ . DF-HRME images show distinct microvascular features at different anatomic sites. Elongated vessels were clearly resolved in DF-HRME images of columnar epithelium (Fig. 6(A)) and squamous epithelium with ulceration (Fig. 6(D)). DF-HRME images of normal squamous epithelium and high-grade squamous intraepithelial lesion (HSIL) show hairpin capillary loops

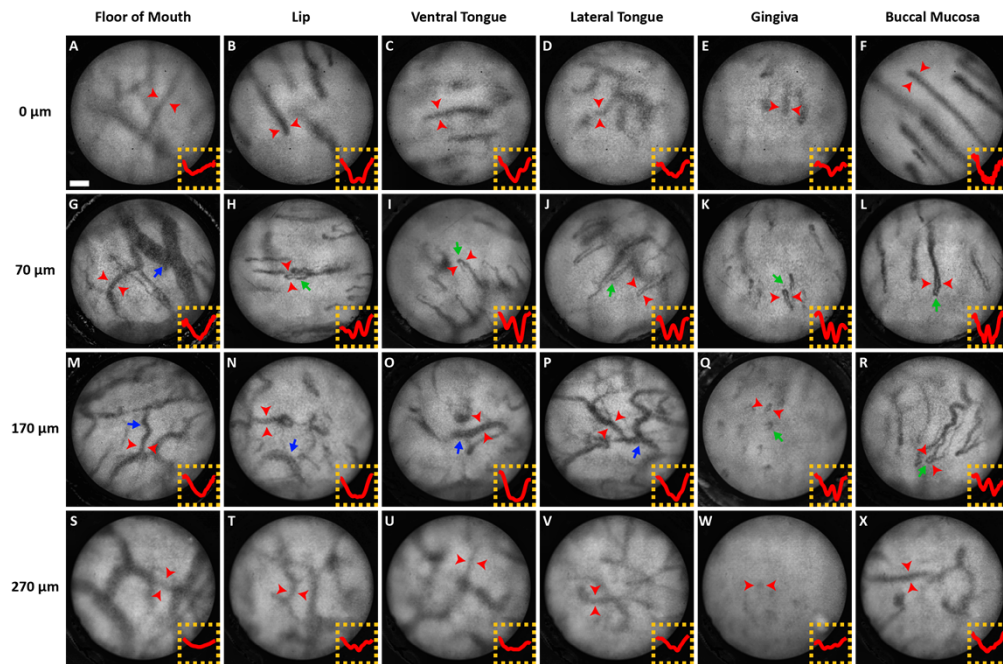


**Fig. 5.** Representative DF-HRME images acquired using probes with different imaging depths (0  $\mu\text{m}$ , 70  $\mu\text{m}$ , 170  $\mu\text{m}$  and 270  $\mu\text{m}$ ) at different anatomic sites in the oral cavity of healthy volunteers. Intensity line profiles of representative microvessels (red arrows) are shown at the bottom right of each panel. Vasculature is in focus and clearly resolved in images acquired by probes with imaging depths of 70  $\mu\text{m}$  and 170  $\mu\text{m}$ . Focused large branching vessels (blue arrows) and hairpin capillary loops (green arrows) are highlighted. (Scale bar: 100  $\mu\text{m}$ )

respectively in Fig. 6(C) and 6(E). As shown in Fig. 6(B), elongated vessels and capillary loops were observed in DF-HRME images of squamocolumnar junction (SCJ).

Representative DF-HRME images obtained at 0 and 70  $\mu\text{m}$  depths from various sites within the cervical specimens with different histopathologic results, together with corresponding histopathology images are shown in Fig. 7. At a representative site of columnar epithelium (Fig. 7(A)), DF-HRME images revealed branch-like vessels, which have large diameters and form a network structure. The vascular patterns observed in DF-HRME images of normal columnar epithelium match the finding in other colposcopy studies, where network-like vessels are found in nonmalignant columnar epithelium [47]. The vascular features were in focus with well-defined morphology when using a bare fiber with an imaging depth of 0  $\mu\text{m}$ , indicating that these vessels are located in the superficial epithelium. This finding was further confirmed by the corresponding histopathology image, which showed the presence of vessels at the superficial surface of the epithelium, as indicated by black arrows. When using the probe with 70  $\mu\text{m}$  imaging depth, the vascular features could still be discerned with good quality. As the columnar epithelium transforms into squamous epithelium at the SCJ, as shown in Fig. 7(B), a combination of branching vessels and hairpin capillary loops is observed in DF-HRME images, and there is a clear boundary between the distinct vascular patterns at the transition between columnar and squamous epithelium. These findings are consistent with the corresponding histopathology image, which confirms the presence of microvessels in both epithelial types; notably, the vessels are close to the surface in the columnar epithelium, and beneath the squamous epithelium.

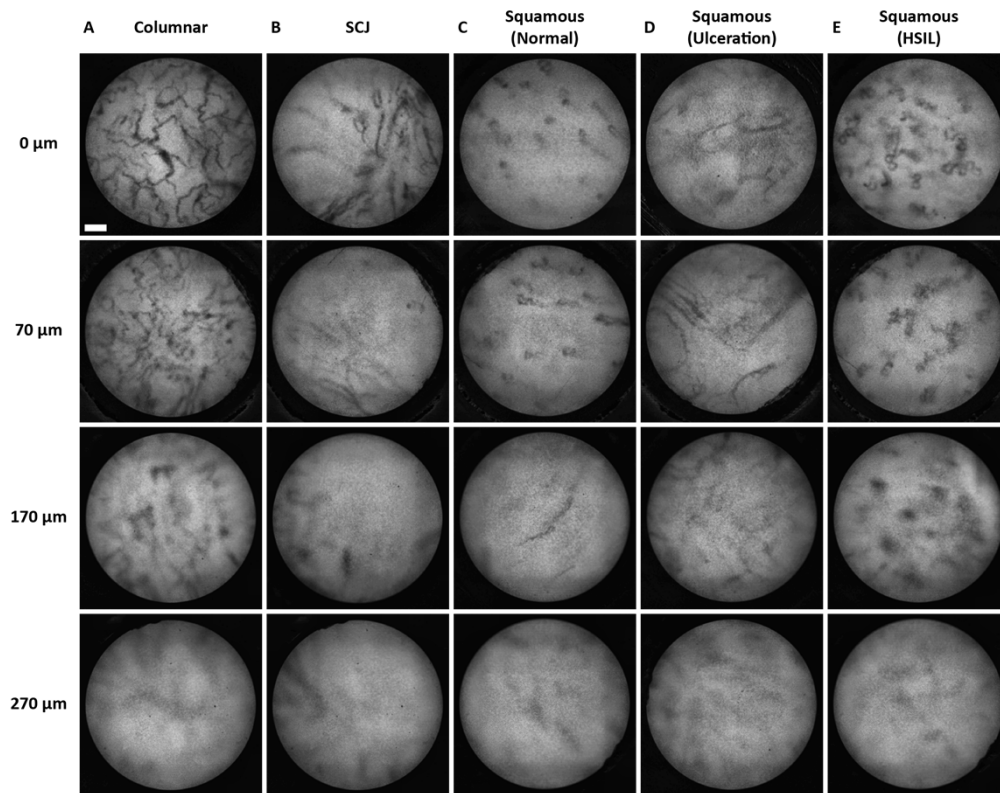


**Fig. 6.** Representative DF-HRME images acquired at different imaging depths from 10 cervical LEEP specimens show various microvascular patterns at different anatomic sites and with different pathologies. In cervical tissue of all types, vasculature is better resolved at imaging depths of 0 and 70  $\mu\text{m}$  compared to depths of 170 and 270  $\mu\text{m}$ . DF-HRME: scanning darkfield high-resolution microendoscope; LEEP: loop electrosurgical excision procedure; SCJ: squamocolumnar junction; HSIL: high-grade squamous intraepithelial lesion. (Scale bar: 100  $\mu\text{m}$ )

In DF-HRME images of normal squamous epithelium (Fig. 7(C)), a few regularly spaced and parallelly distributed hairpin capillaries with small loops are observed. The vascular features match the finding in previous colposcopy studies, where hairpin capillary loop was reported as one representative vascular type observed in normal squamous epithelium [48]. Hairpin capillaries were observed at both imaging depths. The corresponding histopathology image showed normal squamous epithelium but fewer microvessels in the subepithelial region compared to columnar epithelium. In images acquired from the squamous epithelium with ulceration (Fig. 7(D)), elongated vessels with less organized arrangements than Fig. 7(A) were visualized. The corresponding histopathology image revealed ulcerated epithelium with increased vascularization. The DF-HRME image from a representative site of HSIL shown in Fig. 7(E), reveals capillaries with tortuous shape, twisting, termination and arrangement. Similar microvascular patterns were also observed in cervical intraepithelial neoplasia as reported in colposcopy studies [48]. The corresponding histopathology indicated increased vasculature in the lesion, consistent with the high vessel density observed in DF-HRME images. Results of this *ex vivo* clinical study, including images from different precancerous lesions (Fig. 6(E) and 7(E)) and corresponding histopathology, suggest that DF-HRME can image changes in vascular pattern that accompany the development of cervical precancer.

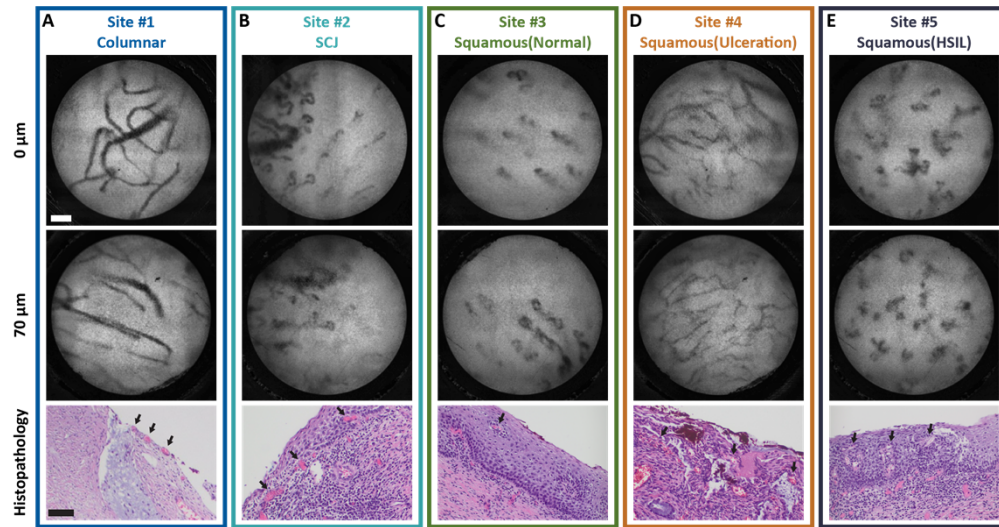


**Fig. 7.** DF-HRME of cervical LEEP specimens clearly reveals distinct microvascular features with different anatomic locations and histopathologic results. DF-HRME images at imaging depths of 0 and 70  $\mu\text{m}$  are shown along with corresponding histopathology images. (A) At a representative site of columnar epithelium, DF-HRME images show branching vessels with a network structure at the superficial surface. The histopathology image confirms the presence of several vessels at the superficial columnar epithelium (arrow). (B) At a representative SCJ site, DF-HRME images reveal the transition of vascular features from branching vessels to individual hairpin capillary loops. Arrows in the histopathology image indicate the depth change of vessels at SCJ. (C) At a representative site of the normal squamous epithelium, hairpin capillaries with small loops that are relatively straight and parallel to each other can be observed at both 0  $\mu\text{m}$  and 70  $\mu\text{m}$  imaging depths in DF-HRME images. The histopathology image shows the presence of a few microvessels in the subepithelial region. (D) At a representative site of squamous epithelium with ulceration, elongated vessels with multiple branches are observed in DF-HRME images. Black arrows in the corresponding histopathology image indicate the presence of dense vasculature in the ulceration area. At a HSIL lesion, the DF-HRME images show tortuous capillary loops. The histopathology image indicates increased vasculature in HSIL. DF-HRME: scanning darkfield high-resolution microendoscope; LEEP: loop electrosurgical excision procedure; SCJ: squamocolumnar junction; HSIL: high-grade squamous intraepithelial lesion. (Scale bars for DF-HRME and histopathology images: 100  $\mu\text{m}$ )

#### 4. Discussion

In this work, we present a fiber-optic microendoscopy system capable of performing high-resolution, label-free and real-time imaging of epithelial microvasculature. Compared to previous fiber-optic fluorescence microscopes, the DF-HRME system consists of two key components: 1) a scanning darkfield microscope that suppresses internal reflection for label-free vascular imaging in reflectance mode, and 2) a coherent imaging fiber bundle with a GRIN lens attachment for extended imaging depth. Through precise alignment and synchronization of the illumination and detection aperture sequences, scanning darkfield imaging is achieved without the need for mechanical scanning, which significantly reduces the complexity and cost of the system (cost of goods < \$5,500). *In vivo* images from the oral cavity demonstrate that scanning darkfield imaging consistently improves image contrast compared to non-scanning widefield imaging; moreover, DF-HRME clearly resolves the morphology of microvessels at different anatomic sites.



Furthermore, we demonstrate that DF-HRME reveals distinct microvascular architecture from different anatomic sites in *ex vivo* cervical specimens, which has potential clinical importance in discriminating neoplastic and non-neoplastic lesions.

Although dysregulated angiogenesis is a highly predictive biomarker for early cancer detection, there remain major obstacles for applying current microvascular imaging technologies in clinical settings. The use of commercially available confocal laser endomicroscopy is limited to tertiary centers due to high cost, and it also requires intravenously injected fluorescein as an exogenous contrast for vascular imaging [20]. While multiple imaging techniques utilize the high optical absorption of hemoglobin as an endogenous contrast mechanism for label-free vascular imaging, their clinical application is often hampered by large form factor, high cost and limited resolution. As demonstrated in the current work, DF-HRME utilizes a thin, flexible and small-form-factor fiber bundle for label-free imaging of microvasculature in high resolution. We validated the imaging performance of DF-HRME by *in vivo* imaging in the oral cavity and *ex vivo* imaging of cervical specimens, and it can be readily adapted for *in vivo* imaging in different body lumens, such as the anal canal, colon, and esophagus. Previous studies have demonstrated *in vivo* application of fluorescence microendoscopes in the anal canal [49], colon [50], and esophagus [50,51] using a similar forward-viewing imaging fiber. These studies validate the potential of adapting the forward-viewing DF-HRME imaging probe for *in vivo* application in these lumens. Furthermore, the cost of goods for the DF-HRME is low, making it possible to deploy in various clinical settings, including medical facilities with limited resources. Our study demonstrates that the optimal imaging depth for visualizing microvasculature varies depending on the specific organ site. DF-HRME imaging probes can approximately indicate the depth of microvessels that are in focus within the depth of field, which can be potentially used as a clinical biomarker for precancer or cancer detection [52]. The current imaging probe design can be adapted for various clinical applications by fabricating probes with different fixed imaging depths. Future research should focus on improving the probe design to enable the imaging depth to be adjusted while preserving valuable features of the current probe design, including its low cost, small form factor, and the ease of disinfection.

We evaluated the capability of DF-HRME to visualize microvascular architecture in cervical lesions by imaging *ex vivo* cervical LEEP specimens. Our preliminary clinical results demonstrated that DF-HRME was able to identify distinct and clinically relevant microvascular patterns at different anatomic sites, which holds potential to assist in detecting precancerous lesions and early cancers. It is important to note that matching the same microvasculature between DF-HRME images and histopathology images is challenging due to different imaging planes for the two sampling methods. To provide a better histological correlation in its 3D context, DF-HRME can be potentially combined with other cross-sectional imaging techniques such as OCT angiography or 3D histopathology techniques. Nevertheless, the observed differences in microvascular features at various anatomic sites and imaging depths are consistent with histopathology images, such as the microvascular pattern transition at the SCJ. Given the promising results, more clinical samples are necessary to fully understand the relationship between microvascular features and the different stages of cancer progression in the cervix. A larger clinical sample size is warranted to perform a more comprehensive assessment of the clinical importance of DF-HRME for cancer detection with statistical significance. Future research will focus on developing diagnostic criteria using microvascular patterns to distinguish normal cervical tissue from precancerous lesions (low-grade and high-grade) as well as early invasive cancer. In addition, studies can also be designed to evaluate the system usability for endoscopic imaging applications in other organ sites.

## 5. Conclusion

In conclusion, we present a low-cost, portable, noninvasive and easy-to-use microendoscope for high-resolution and label-free *in vivo* microvascular imaging. Digital apertures on the DLP and



CMOS sensor are utilized to achieve scanning darkfield imaging with no complex optomechanical components needed. DF-HRME showed consistent ability to resolve microvasculature during *in vivo* imaging of the oral cavities of healthy volunteers, as well as *ex vivo* imaging of cervical LEEP specimens. Preliminary results from the clinical study demonstrated that DF-HRME has the potential to aid in discriminating neoplastic and non-neoplastic cervical lesions. If successful in further studies, this technology could allow for the real-time diagnosis of precancerous lesions without the need for a biopsy. This would decrease patient loss to follow-up and improve cancer prevention and early detection in low-resource settings.

**Funding.** National Institute of Dental and Craniofacial Research (R01DE029590); National Cancer Institute (P30CA016672).

**Acknowledgments.** The authors thank all the healthy volunteers and patients who volunteered to participate in the study. The authors also thank Andrew Kim, Cindy Melendez and Keiry Paiz for coordinating patient recruitment and enrollment. Research reported in this publication was in part supported by the National Institute of Dental and Craniofacial Research of the National Institutes of Health (Grant No. R01DE029590), and United States National Cancer Institute through the MD Anderson Cancer Center Support Grant (Grant No. P30CA016672).

**Disclosures.** The authors declare no competing interests.

**Data availability.** Data underlying the results presented in this paper are not publicly available at this time but may be obtained from the authors upon reasonable request.

## References

1. M. Sathyakumar, G. Sriram, T. R. Saraswathi, and B. Sivapathasundharam, "Immunohistochemical evaluation of mast cells and vascular endothelial proliferation in oral precancerous lesion-leukoplakia," *J. Oral. Maxillofac. Pathol.* **16**(3), 343–348 (2012).
2. T. Sasahira, T. Kirita, M. Kurihara, K. Yamamoto, U. K. Bhawal, A. K. Bosserhoff, and H. Kuniyasu, "MIA-dependent angiogenesis and lymphangiogenesis are closely associated with progression, nodal metastasis and poor prognosis in tongue squamous cell carcinoma," *Eur. J. Cancer* **46**(12), 2285–2294 (2010).
3. N. Kargahi, N. Torabinia, S. M. Razavi, D. Tahririan, H. Kamani, and M. Nazari, "Immunohistochemically detection of angiogenesis in oral pre-cancerous lesions compared with oral invasive carcinomas," *Asian Pac. J. Cancer Prev.* **19**(7), 1805–1808 (2018).
4. D. G. E. Thiem, S. Schneider, N. T. Venkatraman, V. V. Kumar, J. Brieger, B. Frerich, and P. W. Kämmerer, "Semi-quantifiable angiogenesis parameters in association with the malignant transformation of oral leukoplakia," *J. Oral. Pathol. Med.* **46**(9), 710–716 (2017).
5. K. Smith-McCune, Y.-H. Zhu, D. Hanahan, and J. Arbeit, "Cross-Species Comparison of Angiogenesis during the Premalignant Stages of Squamous Carcinogenesis in the Human Cervix and K14-HPV16 Transgenic Mice," *Cancer Res.* **57**(7), 1294–1300 (1997).
6. S. P. Dobbs, P. W. Hewett, I. R. Johnson, J. Carmichael, and J. C. Murray, "Angiogenesis is associated with vascular endothelial growth factor expression in cervical intraepithelial neoplasia," *Br. J. Cancer* **76**(11), 1410–1415 (1997).
7. M. A. Kara, M. Ennahachi, P. Fockens, F. J. W. ten Kate, and J. J. G. H. M. Bergman, "Detection and classification of the mucosal and vascular patterns (mucosal morphology) in Barrett's esophagus by using narrow band imaging," *Gastrointest Endosc.* **64**(2), 155–166 (2006).
8. K. Shibuya, T. Nakajima, T. Fujiwara, M. Chiyo, H. Hoshino, Y. Moriya, M. Suzuki, K. Hiroshima, Y. Nakatani, and I. Yoshino, "Narrow band imaging with high-resolution bronchovideoscopy: A new approach for visualizing angiogenesis in squamous cell carcinoma of the lung," *Lung Cancer* **69**(2), 194–202 (2010).
9. H. Inoue, M. Kaga, H. Ikeda, C. Sato, H. Sato, H. Minami, E. Grace Santi, H. Hayee, and N. Eleftheriadis, "Magnification endoscopy in esophageal squamous cell carcinoma: a review of the intrapapillary capillary loop classification," *Ann Gastroenterol* **28**(1), 41–48 (2015).
10. A. Guida, M. Maglione, A. Crispo, F. Perri, S. Villano, E. Pavone, C. Aversa, F. Longo, F. Feroce, G. Botti, and F. Ionna, "Oral lichen planus and other confounding factors in narrow band imaging (NBI) during routine inspection of oral cavity for early detection of oral squamous cell carcinoma: A retrospective pilot study," *BMC Oral Health* **19**(1), 70 (2019).
11. J. H. Takano, T. Yakushiji, I. Kamiyama, T. Nomura, A. Katakura, N. Takano, and T. Shibahara, "Detecting early oral cancer: narrowband imaging system observation of the oral mucosa microvasculature," *Int. J. Oral Maxillofac. Surg.* **39**(3), 208–213 (2010).
12. J. Laitakari, V. Näyhä, and F. Stenbäck, "Size, shape, structure, and direction of angiogenesis in laryngeal tumour development," *J. Clin. Pathol.* **57**(4), 394–401 (2004).
13. N. Nishiyama, K. Kanenishi, and H. Mori, *et al.*, "Flexible magnifying endoscopy with narrow band imaging for the diagnosis of uterine cervical tumors: A cooperative study among gastrointestinal endoscopists and gynecologists to explore a novel microvascular classification system," *Oncol. Lett.* **14**(1), 355–362 (2017).

14. J. Swangsri, Y. Nakajima, K. Kawada, Y. Tokairin, S. Tomoyoshi, Y. Miyawaki, A. Hoshino, T. Okada, S. Ota, T. Ryotokuji, N. Fujiwara, T. Nishikage, K. Nagai, H. Kawachi, and T. Kawano, "Changes in the microvascular structure of mucosal squamous cell carcinoma of the esophagus and their significance in tumor progression," *J. Med. Dent. Sci.* **60**(4), 83–91 (2013).
15. C. O. Yanez, A. R. Morales, X. Yue, T. Urakami, M. Komatsu, T. A. H. Järvinen, and K. D. Belfield, "Deep Vascular Imaging in Wounds by Two-Photon Fluorescence Microscopy," *PLoS One* **8**(7), e67559 (2013).
16. S. Motamedi, T. Shilagard, and K. Edward, *et al.*, "Gold nanorods for intravital vascular imaging of preneoplastic oral mucosa," *Biomed. Opt. Express* **2**, 1194–1203 (2011).
17. J. Massin, A. Charaf-Eddin, F. Appaix, Y. Bretonnière, D. Jacquemin, B. van der Sanden, C. Monnerneau, and C. Andraud, "A water soluble probe with near infrared two-photon absorption and polarity-induced fluorescence for cerebral vascular imaging," *Chem. Sci.* **4**(7), 2833–2843 (2013).
18. J. D. Lewis, G. Destito, A. Zijlstra, M. J. Gonzalez, J. P. Quigley, M. Manchester, and H. Stuhlmann, "Viral nanoparticles as tools for intravital vascular imaging," *Nat. Med.* **12**(3), 354–360 (2006).
19. S. M. Arribas, C. J. Daly, M. C. González, and J. C. McGrath, "Imaging the vascular wall using confocal microscopy," *J. Physiol.* **584**(1), 5–9 (2007).
20. S. S. Chauhan, B. K. Abu Dayyeh, Y. M. Bhat, K. T. Gottlieb, J. H. Hwang, S. Komanduri, V. Konda, S. K. Lo, M. A. Manfredi, J. T. Maple, F. M. Murad, U. D. Siddiqui, S. Banerjee, and M. B. Wallace, "Confocal laser endomicroscopy," *Gastrointest Endosc.* **80**(6), 928–938 (2014).
21. C. Richardson, P. Colavita, C. Dunst, J. Bagnato, P. Billing, K. Birkenhagen, F. Buckley, W. Buitrago, J. Burnette, P. Leggett, H. McCollister, K. Stewart, T. Wang, A. Zfass, and P. Severson, "Real-time diagnosis of Barrett's esophagus: a prospective, multicenter study comparing confocal laser endomicroscopy with conventional histology for the identification of intestinal metaplasia in new users," *Surg. Endosc.* **33**(5), 1585–1591 (2019).
22. T. Son, J. Lee, and B. Jung, "Contrast enhancement of laser speckle contrast image in deep vasculature by reduction of tissue scattering," *J. Opt. Soc. Korea* **17**(1), 86–90 (2013).
23. V. Kalchenko, D. Israeli, Y. Kuznetsov, and A. Harmelin, "Transcranial optical vascular imaging (TOVI) of cortical hemodynamics in mouse brain," *Sci. Rep.* **4**(1), 5839 (2014).
24. S. M. White, R. Hingorani, R. P. S. Arora, C. C. W. Hughes, S. C. George, and B. Choi, "Longitudinal in vivo imaging to assess blood flow and oxygenation in implantable engineered tissues," *Tissue Eng. Part C Methods* **18**(9), 697–709 (2012).
25. P. K. Upputuri, K. Sivasubramanian, C. S. K. Mark, and M. Pramanik, "Recent developments in vascular imaging techniques in tissue engineering and regenerative medicine," *Biomed. Res. Int.* **2015**, 1 (2015).
26. W. J. Choi and R. K. Wang, "In vivo imaging of functional microvasculature within tissue beds of oral and nasal cavities by swept-source optical coherence tomography with a forward/side-viewing probe," *Biomed. Opt. Express* **5**(8), 2620 (2014).
27. C. Blatter, J. Weingast, A. Alex, B. Grajciar, W. Wieser, W. Drexler, R. Huber, and R. A. Leitgeb, "In situ structural and microangiographic assessment of human skin lesions with high-speed OCT," *Biomed. Opt. Express* **3**(10), 2636–2646 (2012).
28. M. S. Mahmud, D. W. Cadotte, B. Vuong, C. Sun, T. W. H. Luk, A. Mariampillai, and V. X. D. Yang, "Review of speckle and phase variance optical coherence tomography to visualize microvascular networks," *J. Biomed. Opt.* **18**(5), 050901 (2013).
29. V. J. Srinivasan and H. Radhakrishnan, "Optical Coherence Tomography angiography reveals laminar microvascular hemodynamics in the rat somatosensory cortex during activation," *NeuroImage* **102**(P2), 393–406 (2014).
30. X. Zhang, L. Beckmann, D. A. Miller, G. Shao, Z. Cai, C. Sun, N. Sheibani, X. Liu, J. Schuman, M. Johnson, T. Kume, and H. F. Zhang, "In vivo imaging of Schlemm's canal and limbal vascular network in mouse using visible-light OCT," *Invest. Ophthalmol. Vis. Sci.* **61**(2), 23 (2020).
31. D. Chen, W. Yuan, H.-C. Park, and X. Li, "In vivo assessment of vascular-targeted photodynamic therapy effects on tumor microvasculature using ultrahigh-resolution functional optical coherence tomography," *Biomed. Opt. Express* **11**(8), 4316 (2020).
32. K. Liang, O. O. Ahsen, Z. Wang, H.-C. Lee, W. Liang, B. M. Potsaid, T.-H. Tsai, M. G. Giacomelli, V. Jayaraman, H. Mashimo, X. Li, and J. G. Fujimoto, "Endoscopic forward-viewing optical coherence tomography and angiography with MHz swept source," *Opt. Lett.* **42**(16), 3193 (2017).
33. L. M. Wurster, S. Kretschmer, J. Jäger, F. Placzek, L. Ginner, W. Drexler, Ç. Ataman, R. A. Leitgeb, and H. Zappe, "Comparison of optical coherence tomography angiography and narrow-band imaging using a bimodal endoscope," *J. Biomed. Opt.* **25**(03), 1 (2019).
34. S. Hu and L. V. Wang, "Photoacoustic imaging and characterization of the microvasculature," *J. Biomed. Opt.* **15**(1), 011101 (2010).
35. R. Lin, J. Chen, H. Wang, M. Yan, W. Zheng, and L. Song, "Longitudinal label-free optical-resolution photoacoustic microscopy of tumor angiogenesis in vivo," *Quant Imaging Med. Surg.* **5**(1), 23–29 (2015).
36. A. B. E. Attia, G. Balasundaram, M. Moothanchery, U. S. Dinish, R. Bi, V. Ntziachristos, and M. Olivo, "A review of clinical photoacoustic imaging: Current and future trends," *Photoacoustics* **16**, 100144 (2019).
37. F. Yang, Z. Wang, W. Zhang, H. Ma, Z. Cheng, Y. Gu, H. Qiu, and S. Yang, "Wide-field monitoring and real-time local recording of microvascular networks on small animals with a dual-raster-scanned photoacoustic microscope," *J. Biophotonics* **13**(6), 1 (2020).

38. K. Gono, T. Obi, M. Yamaguchi, N. Ohyama, H. Machida, Y. Sano, S. Yoshida, Y. Hamamoto, and T. Endo, "Appearance of enhanced tissue features in narrow-band endoscopic imaging," *J. Biomed. Opt.* **9**(3), 568 (2004).
39. S. C. Ng and J. Y. Lau, "Narrow-band imaging in the colon: Limitations and potentials," *Journal of Gastroenterology and Hepatology (Australia)* **26**(11), 1589–1596 (2011).
40. Y. Ezoe, M. Muto, N. Uedo, H. Doyama, K. Yao, I. Oda, K. Kaneko, Y. Kawahara, C. Yokoi, Y. Sugiura, H. Ishikawa, Y. Takeuchi, Y. Kaneko, and Y. Saito, "Magnifying narrowband imaging is more accurate than conventional white-light imaging in diagnosis of gastric mucosal cancer," *Gastroenterology* **141**(6), 2017–2025.e3 (2011).
41. C. M. Treu, O. Lupi, D. A. Bottino, and E. Bouskela, "Sidestream dark field imaging: The evolution of real-time visualization of cutaneous microcirculation and its potential application in dermatology," *Arch. Dermatol. Res.* **303**(2), 69–78 (2011).
42. G. N. McKay, N. Mohan, I. Butterworth, A. Bourquard, Á. Sánchez-Ferro, C. Castro-González, and N. J. Durr, "Visualization of blood cell contrast in nailfold capillaries with high-speed reverse lens mobile phone microscopy," *Biomed. Opt. Express* **11**(4), 2268 (2020).
43. F. Hu, R. Morhard, H. A. Murphy, C. Zhu, and N. Ramanujam, "Dark field optical imaging reveals vascular changes in an inducible hamster cheek pouch model during carcinogenesis," *Biomed. Opt. Express* **7**(9), 3247 (2016).
44. M. Heger, J. F. Beek, K. Stenback, D. J. Faber, M. J. van Gemert, C. Ince, D. W. Slaaf, G. J. Tangelder, R. S. Reneman, K. Jager, and A. Bollinger, "Darkfield orthogonal polarized spectral imaging for studying endovascular laser-tissue interactions in vivo-a preliminary study," *Opt. Express* **13**(3), 702–715 (2005).
45. Y. Tang, A. Kortum, I. Vohra, M. Othman, S. Dhingra, N. Mansour, J. Carns, S. Anandasabapathy, and R. Richards-Kortum, "Improving nuclear morphometry imaging with real-time and low-cost line-scanning confocal microendoscope," *Opt. Lett.* **44**(3), 654 (2019).
46. Y. Tang and J. Carns, "Line-scanning confocal microendoscope for nuclear morphometry imaging," *J. Biomed. Opt.* **22**(11), 1 (2017).
47. M. Ueki, *Cervical Adenocarcinoma: A Colposcopic Atlas* (Ishiyaku EuroAmerica, Inc, 1985).
48. M. Anderson, J. Jordan, A. Morse, and F. Sharp, *A Text and Atlas of Integrated Colposcopy* (Mosby-Year Book, Inc, 1991).
49. D. Brenes, A. Kortum, J. Carns, T. Mutetwa, R. Schwarz, Y. Liu, K. Sigel, R. Richards-Kortum, S. Anandasabapathy, M. Gaisa, and E. Chiao, "Automated in vivo high-resolution imaging to detect HPV-associated anal precancer in persons living with HIV," *Clin Transl Gastroenterol.* **14**(12), e00558 (2022).
50. M. C. Pierce, P. M. Vila, A. D. Polydorides, R. Richards-Kortum, and S. Anandasabapathy, "Low-cost endomicroscopy in the esophagus and colon," *Am. J. Gastroenterol.* **106**(9), 1722–1724 (2011).
51. M. A. Protano, H. Xu, and G. Wang, *et al.*, "Low-cost high-resolution microendoscopy for the detection of esophageal squamous cell neoplasia: An international trial," *Gastroenterology* **149**(2), 321–329 (2015).
52. J. W. Sellors, R. Sankaranarayanan and International Agency for Research on Cancer, *Colposcopy and Treatment of Cervical Intraepithelial Neoplasia : A Beginner's Manual* (International Agency for Research on Cancer, 2003).